



Damascene-patterned optical anisotropy in integrated photonics

JEFF CHILES,^{1,3} TRACY SJAARDEMA,¹ ASHUTOSH RAO,¹ AND SASAN FATHPOUR^{1,2,*}

¹CREOL, The College of Optics and Photonics, University of Central Florida, Orlando, FL 32816, USA

²Department of Electrical Engineering and Computer Science, University of Central Florida, Orlando, FL 32816, USA

³Currently at the National Institute of Standards and Technology, Boulder, CO 80305, USA

*fathpour@creol.ucf.edu

Abstract: We propose, simulate and experimentally demonstrate a method for realizing spatially-mapped birefringence onto integrated photonic devices and circuits. The fabrication method is based on applying a damascene-like process to dielectric film stacks to form anisotropic optical waveguides. An integrated polarizing beam-splitter (PBS) is realized with unprecedented performance: a record 0.52 octaves of fractional bandwidth (116 THz), maximum on-chip insertion loss of 1.4 ± 0.8 dB, and a minimum extinction ratio of 16 ± 3 dB, pushing it into the realm of wideband spectroscopy and imaging applications. Additionally, photonic structures such as polarization-selective beam-taps and polarization-selective microring resonators are demonstrated.

© 2017 Optical Society of America under the terms of the [OSA Open Access Publishing Agreement](#)

OCIS codes: (130.5440) Polarization-selective devices; (130.3120) Integrated optics devices; (130.3060) Infrared.

References and links

1. R. Nagarajan, J. Rahn, M. Kato, J. Pleumeekers, D. Lambert, V. Lal, H. S. Tsai, A. Nilsson, A. Dentai, M. Kuntz, R. Malendevich, J. Tang, J. Zhang, T. Butrie, M. Raburn, B. Little, W. Chen, G. Goldfarb, V. Dominic, B. Taylor, M. Reffle, F. Kish, and D. Welch, "10 Channel, 45.6 Gb/s per channel, polarization-multiplexed DQPSK, InP receiver photonic integrated circuit," *J. Lightwave Technol.* **29**(4), 386–395 (2011).
2. D. Huang, E. A. Swanson, C. P. Lin, J. S. Schuman, W. G. Stinson, W. Chang, M. R. Hee, T. Flotte, K. Gregory, C. A. Puliafito, and J. G. Fujimoto, "Optical coherence tomography," *Science* **254**(5035), 1178–1181 (1991).
3. Z. Wang, H.-C. Lee, D. Vermeulen, L. Chen, T. Nielsen, S. Y. Park, A. Ghaemi, E. Swanson, C. Doerr, and J. Fujimoto, "Silicon photonic integrated circuit swept-source optical coherence tomography receiver with dual polarization, dual balanced, in-phase and quadrature detection," *Biomed. Opt. Express* **6**(7), 2562–2574 (2015).
4. Z. Wang, B. Potsaid, L. Chen, C. Doerr, H.-C. Lee, T. Nielson, V. Jayaraman, A. E. Cable, E. Swanson, and J. G. Fujimoto, "Cubic meter volume optical coherence tomography," *Optica* **3**(12), 1496–1503 (2016).
5. J. S. Tyo, D. L. Goldstein, D. B. Chenault, and J. A. Shaw, "Review of passive imaging polarimetry for remote sensing applications," *Appl. Opt.* **45**(22), 5453–5469 (2006).
6. S. Tan and R. M. Narayanan, "Design and performance of a multiwavelength airborne polarimetric lidar for vegetation remote sensing," *Appl. Opt.* **43**(11), 2360–2368 (2004).
7. P. Goloub, M. Herman, H. Chepfer, J. Riedi, G. Brogniez, P. Couvert, and G. Séze, "Cloud thermodynamical phase classification from the POLDER spaceborne instrument," *J. Geophys. Res. Atmos.* **105**(D11), 14747–14759 (2000).
8. D. Cornwell, "Space-based laser communications break threshold," *Opt. Photonics News* **27**(5), 24–31 (2016).
9. H. Wu, Y. Tan, and D. Dai, "Ultra-broadband high-performance polarizing beam splitter on silicon," *Opt. Express* **25**(6), 6069–6075 (2017).
10. Z. Su, E. Timurdogan, E. S. Hosseini, J. Sun, G. Leake, D. D. Coolbaugh, and M. R. Watts, "Four-port integrated polarizing beam splitter," *Opt. Lett.* **39**(4), 965–968 (2014).
11. D. Dai and H. Wu, "Realization of a compact polarization splitter-rotator on silicon," *Opt. Lett.* **41**(10), 2346–2349 (2016).
12. B. Little, "Integrated optics polarization beam splitter using form birefringence," U.S. patent US20060120657 A1 (2006).
13. X. Sun, J. S. Aitchison, and M. Mojahedi, "Realization of an ultra-compact polarization beam splitter using asymmetric MMI based on silicon nitride / silicon-on-insulator platform," *Opt. Express* **25**(7), 8296–8305 (2017).
14. Y. Shani, C. H. Henry, R. C. Kistler, R. F. Kazarinov, and K. J. Orlowsky, "Integrated optic adiabatic polarization splitter on silicon," *Appl. Phys. Lett.* **56**(2), 120–121 (1990).

15. D. Dai, J. Bauters, and J. E. Bowers, "Passive technologies for future large-scale photonic integrated circuits on silicon: polarization handling, light non-reciprocity and loss reduction," *Light Sci. Appl.* **1**(3), e1 (2012).
16. E. Kapon, "Polarizing optical waveguides," U.S. patent US4869569 A (1989).
17. Y. Suzuki, H. Iwamura, and O. Mikami, "TE/TM mode selective channel waveguides in GaAs/AlAs superlattice fabricated by SiO₂ cap disordering," *Appl. Phys. Lett.* **56**(1), 19–20 (1990).
18. Y. Suzuki, H. Iwamura, T. Miyazawa, and O. Mikami, "A novel waveguided polarization mode splitter using refractive index changes induced by superlattice disordering," *IEEE J. Quantum Electron.* **30**(8), 1794–1800 (1994).
19. O. Watanabe, M. Tschimori, A. Okada, and H. Ito, "Mode selective polymer channel waveguide defined by the photoinduced change in birefringence," *Appl. Phys. Lett.* **71**(6), 750–752 (1997).
20. M.-C. Oh, M.-H. Lee, and H.-J. Lee, "Polymeric waveguide polarization splitter with a buried birefringent polymer," *IEEE Photonics Technol. Lett.* **11**(9), 1144–1146 (1999).
21. S. R. Forrest, F. F. So, and D. Y. Zang, "Polarization-selective integrated optoelectronic devices incorporating crystalline organic thin films," U.S. patent US5172385 A (1992).
22. R. Sun, J. Cheng, J. Michel, and L. Kimerling, "Transparent amorphous silicon channel waveguides and high-Q resonators using a damascene process," *Opt. Lett.* **34**(15), 2378–2380 (2009).
23. M. H. P. Pfeiffer, A. Kordts, V. Brasch, M. Zervas, M. Geiselmann, J. D. Jost, and T. J. Kippenberg, "Photonic damascene process for integrated high-Q microresonator based nonlinear photonics," *Optica* **3**(1), 20–25 (2016).
24. M. Born and E. Wolf, *Principles of Optics: Electromagnetic Theory of Propagation, Interference and Diffraction of Light*, (Elsevier, 1980).
25. S. Jahani and Z. Jacob, "Transparent subdiffraction optics: nanoscale light confinement without metal," *Optica* **1**(2), 96 (2014).
26. R.-C. Tyan, A. A. Salvekar, H.-P. Chou, C.-C. Cheng, A. Scherer, P.-C. Sun, F. Xu, and Y. Fainman, "Design, fabrication, and characterization of form-birefringent multilayer polarizing beam splitter," *J. Opt. Soc. Am. A* **14**(7), 1627 (1997).
27. Y. Tan, S. Chen, and D. Dai, "Polarization-selective microring resonators," *Opt. Express* **25**(4), 4106–4119 (2017).
28. B. Shen, R. Polson, and R. Menon, "Increasing the density of passive photonic-integrated circuits via nanophotonic cloaking," *Nat. Commun.* **7**, 13126 (2016).
29. D. G. Rabus, *Integrated Ring Resonators* (Springer, 2007).
30. M. F. Duarte, M. A. Davenport, D. Takhar, J. N. Laska, T. Sun, K. F. Kelly, and R. G. Baraniuk, "Single-pixel imaging via compressive sampling," *IEEE Signal Process. Mag.* **25**(2), 83–91 (2008).

1. Introduction

Polarization-diverse transmitter and receiver architectures are becoming increasingly prevalent in modern integrated photonic systems. A variety of applications benefit directly from this approach; the most well-established being high-bandwidth telecommunications [1]. Polarization diversity potentially enables a doubling of data bandwidth for a modest increase in chip size and little additional complexity. Typical components for this purpose include polarizers, polarizing beam-splitters (PBS) and polarization-splitter-rotators (PSR). Polarization diversity also has significant benefits for photonic systems targeted at sensing and imaging applications such as optical coherence tomography [2–4].

Another application for polarization-diverse integrated photonics is in remote spectroscopy. Remote spectroscopy is a metrology technique applicable to many fields of study, such as environmental monitoring, satellite reconnaissance and planetary science. The merging of polarization-dependent information with images elucidates many details, and the combined study of spectral and polarimetric information in a scene is referred to as spectropolarimetric imaging [5]. Polarimetric light detection and ranging (LIDAR), leveraging dual lasers at 532 and 1064 nm wavelengths, has been used in the study of the vegetation canopy, the structure of which has significant implications in the study of microclimates, as well as large-scale climate change [6]. In atmospheric studies, optical polarimetry allows the precise determination of the phase state of clouds due to the polarization-dependent scattering of water crystals; the POLDER spaceborne instrument successfully conducted such measurements over a spectral band from 443 to 865 nm [7]. Future spaceborne instruments will benefit greatly from the size, weight and power reductions achievable through photonic integration of key subsystems [8].

Still, significant advancements must be made beyond the state-of-the-art for integrated photonic polarization-selective technology. To date, high-efficiency integrated PBS devices

have been demonstrated with up to ~140 nm bandwidth (17 THz or 0.13 octaves) with a maximum excess loss of 1.0 dB [9]. A variety of techniques, such as mode-evolution, asymmetric or bent directional couplers, dielectric overlayers, multiple-material waveguides have been explored for the entire class of polarization-selective devices [10–14]. A more general review of polarization-management approaches is available in [15]. Such devices generally take advantage of the dissimilar electric field distribution inherent to the TE and TM modes of the waveguides involved, which in turn leads to modal birefringence. Consequently, their cross-sections are specifically engineered to enhance this effect. However, the reliance on core-cladding modal dispersion effects inevitably leads to bandwidth limitations on either side: as the wavelength becomes shorter, the TE/TM polarization modes are more strongly confined and less differentiated, and on the long-wavelength side, rapid changes in the modal distribution take over as they enter the weak-confinement regime, and possibly approach cutoff, depending on the geometry.

However, to implement an integrated polarimetric remote sensing system, polarization splitting (either through a splitter-rotator or a beam splitter) must be achieved over a broad bandwidth, typically on the order of an octave in fractional bandwidth [6,7], without incurring excess insertion loss. Although a broad bandwidth could ostensibly be obtained by demultiplexing different spectral bands and implementing a specific PBS design for each band, this entails a complete duplication of the receiver circuit, additional losses, and the merging of multiple signals from the detectors. An additional challenge is the lack of high-index contrast integrated photonic platforms (such as silicon, upon which the most successful polarization diversity technology has relied) that are transparent in the visible spectrum, where many atmospheric studies are conducted. In this work, we introduce a powerful integrated photonic technique capable of meeting these challenges and opening the path for compact, spaceborne polarimetric instrumentation.

1.1 Proposed scheme for on-chip polarization management

The essence of the proposed scheme is manipulating the anisotropy of the waveguiding material itself, rather than manipulating its modal birefringence. Consider a waveguide with a core consisting of some uniaxial anisotropic material with the extraordinary axis pointing in the vertical direction (perpendicular to the plane of the substrate). The TE and TM modes of this waveguide experience a birefringence, which remains even as the wavelength becomes shorter and the mode is strongly confined, in contrast to the behavior of isotropic-core waveguides, where they become less birefringent. If the anisotropy could be adjusted spatially across the chip, or simply “turned off” in some waveguides and not in others, it could be used for polarization-selective operations. This concept resembles selective disordering of quantum wells to tune the anisotropy in semiconductor waveguides [16,17]. By controlling the spatial distribution of material anisotropy on the chip, one can design devices that exploit transitions between different materials. This was later used to demonstrate a PBS [18]. The variable anisotropy concept has also been explored by a limited number of other groups using various approaches such as polymers [19,20] and organic crystals [21]. No broadband polarization-selective devices have been achieved with these approaches, which suffer from poor compactness, fabrication complexities or limited environmental stability due to the choice of materials; additionally, the lack of vertical symmetry in the structures limits their bandwidth.

We propose a novel approach to addressing all these issues by employing a variation of the so-called photonic damascene process [22,23] along with precisely engineered dielectric film stacks. The material anisotropy is derived from a multilayer stack (MLS) consisting of alternating layers (deep-sub-wavelength thickness, t_L and t_H) of, for example, silicon dioxide (SiO_2) (L , low index) and silicon nitride (Si_3N_4) (H , high index), exhibiting form-birefringence in the refractive index as described below by the effective medium theory [24]:

$$n_{\text{eff},TE}^2 = fn_H^2 + (1-f)n_L^2, \quad (1)$$

$$\frac{1}{n_{\text{eff},\text{TM}}^2} = \frac{f}{n_H^2} + \frac{(1-f)}{n_L^2}, \quad (2)$$

$$t_{H,L} \ll \lambda_H, \quad (3)$$

where n is the refractive index, and f is the fill fraction of the high-index material in the MLS. This is a valid approximation given Eq. (3), when the thickness of the layers is much smaller than the wavelength of light inside the medium of high index (λ_H). Birefringence is observed in the material refractive index due to the different behavior of TE- and TM-polarized waves. These so-called “metamaterial” stacks have been exploited for their anisotropic properties to modify the behavior of evanescent fields of waveguide claddings [25] and to construct a thin-film (non-integrated) PBS [26]. Vertical gratings have alternatively been investigated for integrated PBS [12], albeit with limited bandwidth and limited dimensional control.

Now imagine a waveguide [Fig. 1(a)] with a silicon oxynitride (SiON) core and an MLS cladding with refractive indices, as indicated in the figure, satisfying the following conditions:

$$n_{\text{core}} > n_{\text{eff},\text{TM}}, \quad (4)$$

$$n_{\text{core}} < n_{\text{eff},\text{TE}}, \quad (5)$$

$$n_{\text{clad}} < n_{\text{core}}. \quad (6)$$

If the MLS cladding material is constructed such that Eqs. (4)-(6) are satisfied through Eqs. (1) and (2), the waveguide displays intrinsic single-polarization behavior, in that TE-polarized light will become anti-guided due to the negative index contrast, and TM-polarized light will be guided normally. Similarly, if the core and cladding materials are simply swapped in place such that the core is MLS and the cladding is the isotropic material with n_{core} [Fig. 1(b)], the waveguide will only guide TE-polarized light.

The proposed approach indeed allows both of these arrangements, and more, to be achieved in the same process, as follows. The MLS is first deposited on an oxidized silicon substrate. Next, the anisotropy is “mapped” on the surface by etching the MLS in some areas and then filling it with SiON or SiO₂ as core or cladding materials. Etch-back techniques are used to restore surface flatness after the etching and refill deposition steps. A variety of unique waveguiding “states” may be realized, which are summarized in Fig. 1, along with the simplified fabrication process.

The states are divided into fundamental and hybrid types. The fundamental states include TE-only (E), TM-only (M) and bipolarized (B). They consist of one core material with symmetric claddings of another material. The hybrid states, which each use two different core materials, include the symmetric coupled hybrid (SCH), asymmetric coupled hybrid (ACH) and asymmetric split hybrid (ASH). In each fundamental and hybrid state, a different relation exists between the TE and TM modes. For example, in the ACH hybrid state, the TE mode is concentrated in the MLS core due to the higher refractive index, whereas the TM mode is concentrated in the SiON core, due to the low refractive index it experiences in the MLS [Fig. 1(e)]. The polarization-selective behavior of the hybrid states is robust the confinement factor, waveguide geometry tolerances, and even some degree of variability in the refractive indices; it is furthermore compatible with the relatively low-index contrast and spectrally broadband silicon nitride platform.

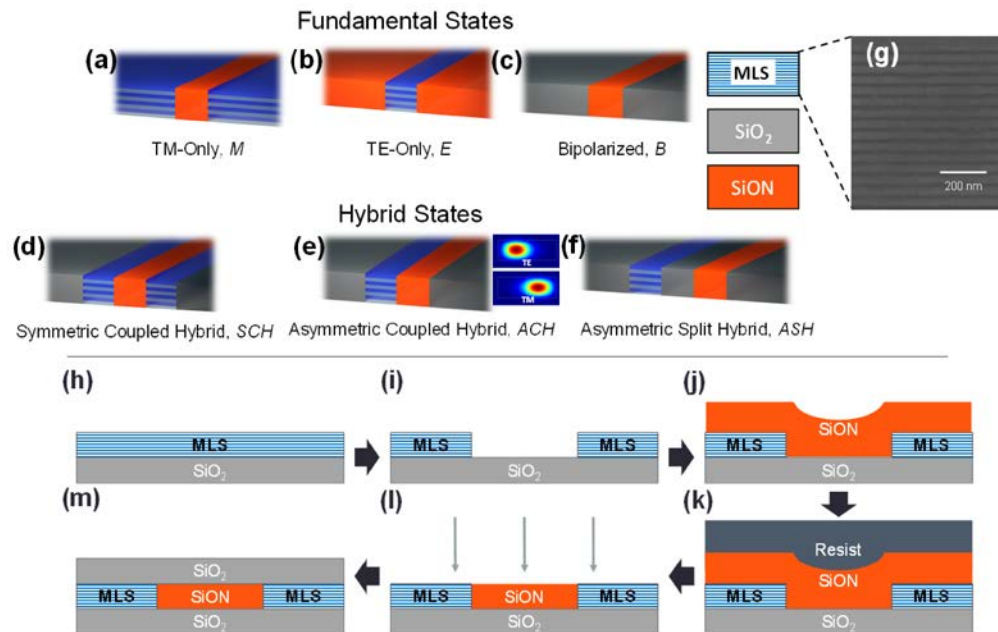


Fig. 1. Fundamental and hybrid waveguide arrangements used in this platform. In (e), the inset to the right shows simulated intensity distributions for TE- and TM-polarized light for the ACH state, illustrating how each polarization-mode is tightly confined to the respective region of greater effective index. (g) Scanning-electron micrograph (SEM) of the fabricated MLS cross-section. The apparent roughness is a result of wet-etching performed to enhance the visible contrast of the layers. (h-m) Simplified fabrication flow: (h) MLS deposition, (i) etching of trenches in the MLS, (j) refill of trenches with SiON, (k) planarization with resist, (l) etch-back with plasma, and (m) top-cladding SiO₂ deposition.

1.2 Design approach

Now, we consider how to apply this to the goal of achieving broadband and efficient polarization-selective devices. In this platform, light can start in any one of the fundamental states, generally in B for incoming light of an indeterminate polarization. Next, to parse the TE and TM modes, a transition may be made to one or more of the hybrid states (such as ACH or ASH), which will result in a new polarization-mode distribution. Finally, it undergoes a transition back to another fundamental state to resume transmission elsewhere on the chip. In the following sections, devices such as PBS and polarization-selective beam-taps and microring resonators are designed and simulated using this simple approach. In principle, polarization rotators are also achievable through standard design approaches in this technology, although they are not a necessary component for remote spectroscopy applications.

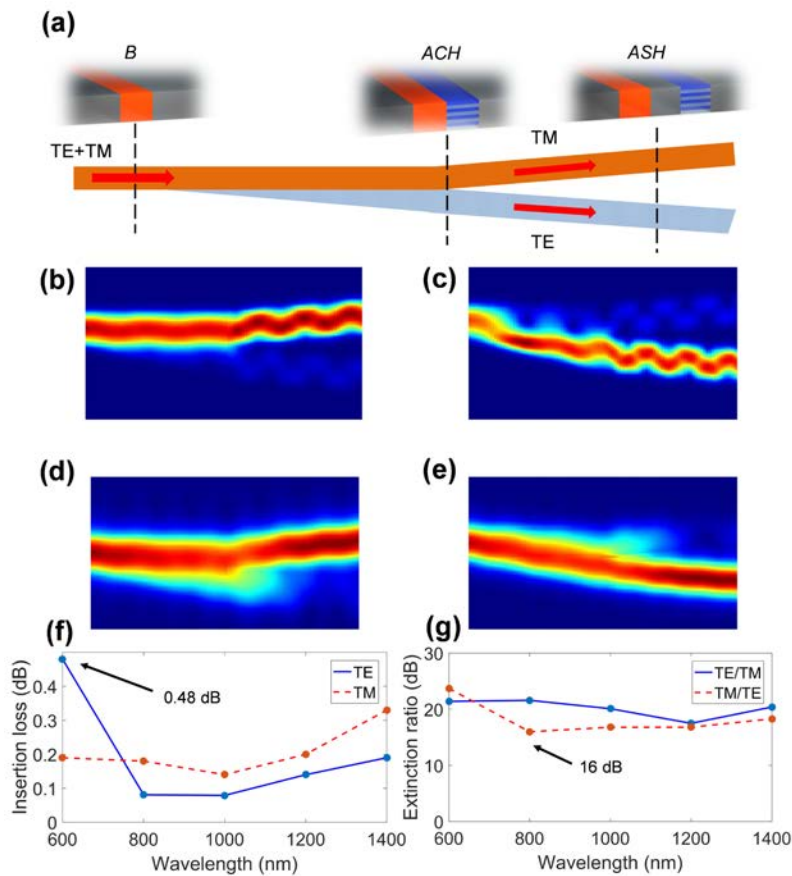


Fig. 2. Polarizing beam splitter design and simulations. (a) Design employing state transitions (whitespace is SiO₂ cladding). (b-d) Simulated normalized electric field (top-view) of the PBS for (b,c) $\lambda = 600$ nm, (d,e) $\lambda = 1400$ nm; (b,d) TM-polarized input, and (c,e) TE-polarized input. (f) Simulated insertion loss spectrum; (g) simulated ER spectrum.

2. Simulations

2.1 Polarizing beam splitter

The PBS consists of the following sequence of states: B – ACH – ASH – B. The approach for designing a PBS is now detailed [Fig. 2]. It is assumed that the input state is B, such that it is bipolarized. Next, a transition is made to the hybrid ACH state mentioned earlier [Fig. 1(e)], which forces the TE and TM modes into separate core regions. Afterward, a transition is made to the ASH state by introducing a “wedge” of silicon dioxide cladding in between the two cores. The B – ACH transition length is 60 μm , the full wedge angle for the ACH – ASH transition is 1°, and the maximum width of the SiON and MLS cores is 1.4 μm , each. The PBS is $\sim 121 \times 5 \mu\text{m}^2$, including the output wedge, not including waveguide width-adjustment tapers. The gap between the SiON and MLS cores is gradually widened until they do not interact. Finally, at the output, the MLS core in the TE arm is replaced with SiON (not pictured) to be compatible with ordinary bus waveguides on the chip. Thus, the output state is again B for both the TE and TM arms, with the two polarization modes efficiently diverted into their respective paths.

The proposed PBS design is simulated in Lumerical MODE Solutions using the eigenmode expansion (EME) algorithm, incorporating an effective anisotropic material (with refractive index $n_{\text{eff,TE}}$ or $n_{\text{eff,TM}}$ for TE or TM light, respectively) for the MLS to avoid the

prohibitive meshing requirements for modeling each layer of the stack. The refractive indices of the different films were measured with prism-coupling at several wavelengths to obtain their dispersion, which was then incorporated into the model. Simulations are conducted by injecting TE or TM light into the B-type input port and monitoring the extinction ratio (ER) and insertion loss at the TE and TM output ports. The performance is examined at $\lambda = 600 - 1400$ nm. The normalized electric field plots are shown in Figs. 2(b)-2(e) for all cases, and the performance is summarized in Figs. 2(f) and 2(g). Across the span from $\lambda = 600$ to 1400 nm, it is observed that the insertion loss remains below 0.5 dB and the ER is always greater than 16 dB. Some multimode oscillation is visible on the output ports at shorter wavelengths; this results from partial mode-conversion in the taper and Y-junction portions. Consequently, the insertion loss is seen to increase at $\lambda = 600$ nm. This may be readily addressed in the future by implementing more refined splitter geometries incorporating curved Y-junctions and parabolic widening profiles. However, it is notable that the PBS operation is still effective at shorter wavelengths, despite the waveguides supporting multiple spatial modes.

2.2 Polarization-selective beam-taps and microring resonators

For applications such as polarimetric remote spectroscopy, it may be desired to construct resonant cavities that have light of only one polarization enter a resonant mode, to apply a spectral filtering profile to that particular polarization state. This is referred to as a polarization-selective microring resonator [27]. A wide optical bandwidth in such a device is important for spectroscopic applications.

This approach provides a means of realizing extremely broadband, low-insertion-loss PSMRs. The design of a PSMR (shown schematically in Fig. 3(a)) follows a similar procedure to that of the PBS. It can be achieved in a B – ASH – B transition, as the bus waveguide crosses the ring cavity waveguide. As with the PBS, the polarization splitting is achieved by using different core materials for the TE and TM ports. For a TE-selective PSMR, the core material in the ring waveguide should thus be MLS, and the core material in the bus should be SiON. Also, the transition to and from the ASH state should allow the mode to gradually evolve. This follows from the use of a gradually widened MLS core in the previous PBS design. Since there is now a gap of SiO₂ cladding separating the bus and the ring waveguides in the PSMR, this can instead be implemented by gradually tapering down and up the width of the ring waveguide. The degree of tapering and the gap allow control over the polarization-dependent coupling ratio (PDCR) and the power coupling coefficient, respectively. The bus and ring waveguide nominal widths are 0.9 μm , the ring radius is 100 μm , and a width taper-down to 700 nm is applied in the ring waveguide by “clipping” the bottom portion. An edge-to-edge gap of 700 nm was used in the clipped waveguide region.

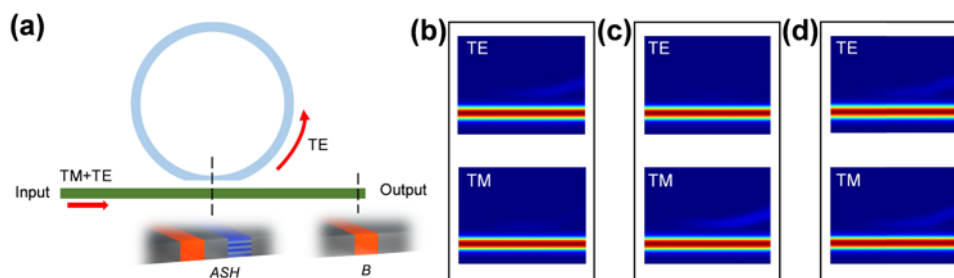


Fig. 3. Polarization-selective beam-tap/microring-resonator design and simulations. (a) Schematic top view of the proposed design approach for a TE-selective microring resonator. Whitespace is the SiO₂ cladding. (b-d) Simulated normalized electric field profile from a top-view of beam-taps for the (b) TE-selective design, (c) TM-selective design, and (d) SiON-core-only design (non-selective).

Simulations are conducted at $\lambda = 850$ nm for TE- and TM-polarized incoming light, for both the TE-selective and TM-selective PSMR cases. Additionally, the case of a purely isotropic core material (SiON) in both the ring and bus waveguides is examined to provide a reference. The simulation is limited to the coupling section. The two-dimensional normalized electric field profiles are shown in Figs. 3(b)-3(d). The key metric of the polarization-dependent coupling ratio (PDCR) is defined simply as the ratio of power coupling coefficient into the tap-off port (or into the ring cavity, alternatively) for one polarization state, divided by the power coupling coefficient into the tap-off port for the other polarization state. In a “TE-selective” PSMR, for instance, the ratio would be P_{TE}/P_{TM} , where P is the power coupling coefficient into the tap-off port. PDCRs of 14.5, 23.4 and 0.42 dB were observed for the TE-selective, TM-selective and non-selective (matched-core materials) cases, respectively.

The small PDCR for the non-selective case compared to that of the selective rings illustrates the effectiveness of this approach, and confirms the effect is attributable to the anisotropic index contrast. In some ways, this device’s engineered control over coupling coefficients resembles the recent use of deep-subwavelength structures with a different goal of increasing the density of nanophotonic components [28]. Next, devices are prepared for testing of the PBS and PSMR designs, and are characterized in the following sections.

3. Fabrication and characterization

TAP samples are prepared for testing of the PBS and PSMR designs, as follows. An MLS consisting of 15 pairs of $\text{Si}_3\text{N}_4/\text{SiO}_2$ layers [Fig. 1(g)] is optimized in fill fraction to give a TE refractive index of 1.71 and a TM refractive index of 1.64. The total thickness of the MLS is approximately 700 nm. Prism-coupling measurements show intrinsic MLS material loss of 4-5 dB/cm at $\lambda = 633$ nm. Next, the SiON film deposition is optimized to give a refractive index of 1.68. The MLS is deposited on an oxidized silicon substrate.

Devices are fabricated by patterning and etching trenches to define regions where SiON or SiO_2 are filled in. As follows, parts of the fabrication method resemble the damascene process employed in other integrated photonic platforms [22,23]. A 700-nm-thick MLS core deposited via plasma-enhanced chemical vapor deposition (PECVD) on oxidized silicon acts as the initial device layer. First, electron-beam lithography is used to pattern a resist mask (ZEP 520, ZEON Corp.) to define where SiON material will replace it. The MLS is fully etched with CHF_3/SF_6 chemistry. After resist stripping, the trenches are re-filled with a thick layer of ~ 1.8 μm SiON using PECVD. The uneven SiON film is planarized with 1 μm of photoresist (Microposit S1805), and then etched halfway through the SiON thickness with CHF_3/O_2 chemistry giving nearly 1:1 selectivity between the resist and SiON. The coating and etch-back are repeated, and the etch is terminated at the top of the MLS. Another lithography and pattern etching is conducted (using CHF_3 chemistry) to define trenches where SiO_2 cladding will be filled in. Afterward, the new trenches are refilled and the surface is top-cladded with PECVD SiO_2 to symmetrize the device layer.

3.1 Polarizing beam splitter

A chip layout is created to allow robust testing of the earlier proposed PBS design. An example propagation path for a PBS test device is given in Fig. 4(a). A common input waveguide 1.5 μm -wide is first tapered down to 0.7 μm and propagated for 300 μm to extinguish most higher-order mode content. Then, it passes through a 50:50 Y-junction splitter into a “device” and a “reference” path. In the device path, the waveguide width is tapered to the appropriate value for the PBS, and then back down to 0.7 μm afterward to allow a larger separation between the TE and TM ports. Finally, it is tapered up to 1.5 μm for low-loss propagation to the output ports. In the reference arm, the waveguide is tapered up to the 1.5 μm output width after a short propagation length to provide appropriate path length

matching between the reference and the device path. The propagation losses are canceled out in each measurement due to the path length matching between the ports.

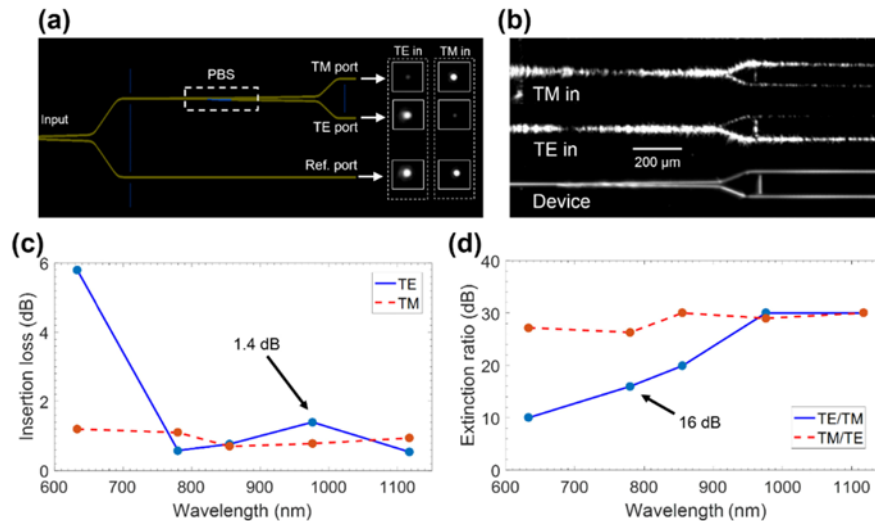


Fig. 4. Device layout and characterization results for polarizing beam-splitter. (a) Top-view schematic of the device layout for testing the PBS, showing the common input bus splitting into the reference and PBS output paths. An example measurement of a port power measurement via top-view imaging is also included ($\lambda = 855$ nm). (b) Top-view from a camera showing scattered light from the PBS arms as TE and TM input polarizations are selected; (c) Experimental insertion loss spectrum observed from the PBS with maximum in-band loss highlighted; (d) Experimental ER spectrum, with minimum in-band value highlighted.

For PBS characterization, light is coupled in through a $20\times$ objective lens from free-space laser sources at $\lambda = 633, 780, 855, 976$ and $1,117$ nm. The input light is polarized immediately after the source with a Glan-Taylor polarizer. An optical micrograph of a fabricated PBS and the fan-out from the device is shown in Fig. 4(b). Light scattering from the output facets (which are terminated in the middle of the chip) is imaged from a top view with a digital camera, such that the TE, TM and reference ports are all visible. We note that the facets are physically identical for all ports (having been prepared with simultaneous plasma etching), such that the scattering behavior is also identical. The optical power in each port is thus proportional to the integral of the intensity profile of the scattered light from each port [Fig. 4(a)]. The image of the facets occupies only a narrow arc within the camera's overall field-of-view, so that the uniformity is not compromised. For calculation of insertion losses, the brightness is always adjusted to avoid saturation of the pixels. Several measurements are conducted when necessary and averaged to obtain the final results. The uncertainty in all PBS measurements is ± 0.8 dB for insertion losses and ± 3 dB for ERs.

Table 1. Comparison of experimental integrated polarizing beam splitter performance

Reference	Platform	Bandwidth (octaves)	Max. insertion loss (dB)	Min. extinction ratio (dB)	Footprint
H. Wu <i>et al.</i> [9]	SOI	0.13	1.0	20	$6.9 \times 20 \mu\text{m}^2$
This work	SiN	0.52	1.4	16	$5 \times 121 \mu\text{m}^2$

The fabricated PBS achieved $\text{ER} > 16$ dB and maximum on-chip insertion losses of 1.4 ± 0.8 dB over a 337 nm span of $\lambda = 780 - 1,117$ nm, representing a fractional bandwidth of 0.52 octaves and a frequency bandwidth of 116 THz. A minimum ER (considering both TE/TM and TM/TE) of 16 ± 3 dB is achieved over the same bandwidth. Furthermore, the ER exceeds 25 dB at longer wavelengths, and the device bandwidth likely extends further in that direction. For the measurements at 633 nm, the high loss most likely results from the

conversion of some input light into higher-order modes, which are immediately filtered at the output of the PBS. We have tabulated the key performance metrics of our device and the best-performing broadband integrated PBS demonstrated to date [9] in Table 1. Our device has comparatively higher losses and a slightly reduced extinction ratio, but operates over a bandwidth that is four times wider in octave-space, and more than six times wider in frequency space (116 THz vs. 17 THz).

There is still a discrepancy between the observed and the simulated performance. Possible factors include aspect-ratio dependent etching (ARDE) effects, or imperfect planarization (we observe a topography of 200 nm near trenches). These issues could have particularly affected the Y-junction in the PBS, resulting in the higher loss at shorter wavelengths from multimode conversion. In the future, this could be improved with chemical-mechanical polishing (CMP).

3.2 Polarization-selective beam-taps and microring resonators

Another chip is fabricated to assess the performance of the PSMR and PSBT designs proposed earlier. The PSBTs are tested by coupling in light at $\lambda = 633, 780$ and 855 nm, using essentially the same approach as for the PBS, although an aspheric lens is employed for improved focusing on the waveguide facet. Multiple exposure times and a careful gain curve calibration are employed to enhanced the camera sensitivity. An example chip layout schematic is shown in Figs. 5(a) and 5(b), where the common input is split into device and reference paths. In the device path, it is further split and diverted into a TE-selective and a TM-selective PSBT, each having a tap and a bus port. The tap power coupling coefficient is used for the PDCR measurement.

The TM- and TE-selective rings of $100\text{-}\mu\text{m}$ -radii are tested with a polarized single-longitudinal-mode vertical-cavity surface-emitting laser (VCSEL) source at $\lambda = 855$ nm (Thorlabs CPS850V), oriented at 45° with respect to the plane of the chip. The ring resonators are identical in structure to the fabricated set of PSBTs, only that the tap port is closed on itself to form the resonant cavity [Fig. 5(b)]. The input light is polarized in the horizontal and vertical directions as required with a Glan-Taylor polarizer. To sweep the laser through the ring resonances, it is thermally tuned from room temperature to 50°C ; the thermistor voltage-to-temperature-to-wavelength characteristic curve is calibrated prior to measurements using an optical spectrum analyzer (OSA). Light is coupled onto the chip via a $20\times$ objective lens, and measured at the output in the same method used for the PBS, but using a time-lapse of images to accumulate the transmission spectrum.

Table 2. Experimental polarization-selective beam-tap performance.

Wavelength (nm)	Device type	TE coupling coefficient	TM coupling coefficient	PDCR, dB
780	TE-selective	2.65%	0.60%	6.5 ± 1
	TM-selective	0.09%	2.22%	14 ± 1
855	TE-selective	2.77%	0.78%	5.5 ± 1
	TM-selective	0.21%	1.83%	9.4 ± 1

The transmission spectra through TM- and TE-selective PSMRs across a full sweep of the laser wavelength are plotted in Figs. 5(c) and 5(d). When necessary, the spectra are corrected for slow drifts in the input power via a spline function to remove an overall tilt. Each transmission spectrum trace is fitted to the characteristic response of a notch resonance [29]. The data are summarized in Table 2. The best devices employed an edge-to-edge coupling gap of 600 nm at the middle of the coupler section. At $\lambda = 633$ nm, no useful PDCR is obtained; this may be due to increased sensitivity to aspect-ratio dependent etching in the narrow gap. However, a $\text{PDCR} > 5.5 \pm 1$ dB, and up to 14 ± 1 dB, is maintained at $\lambda = 780$ and 855 nm. This measurement provides experimental confirmation that strong polarization dependence can be designed into photonic devices through damascene patterning of multilayer stacks.

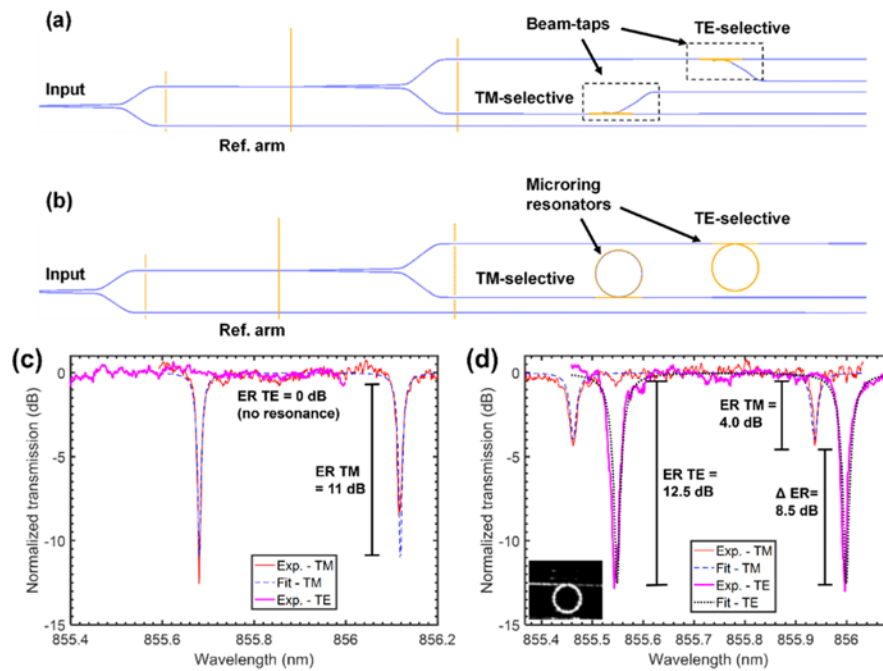


Fig. 5. Polarization-selective beam-taps and microring resonators. (a,b) Device layout for: (a) Beam-taps; (b) Microring resonators. The same geometrical parameters are applied to the TM- and TE-selective PSBTs in a given measurement path (i.e., waveguide width, coupling gap); only the composition of the bus and tap waveguide cores (SiON or MLS) are swapped as dictated by the design. Radius = 100 μm . Vertical lines are etched trenches to prevent light coupled into slab waveguide modes from interfering with the measurements. (c-d) Experimentally measured transmission spectra for polarization-selective microring resonators: (c) TM-selective PSMR. (d) TE-selective PSMR, showing the resonances for TM- and TE-polarized input light and the relative ERs. Inset: top-view infrared micrograph of a PSMR on-resonance.

Next, the transmission spectra of the PSMRs [Figs. 5(c) and 5(d)] are characterized utilizing a narrow-linewidth laser centered at 855 nm. A peak loaded quality factor of $47,000 \pm 5,000$ is observed in the case of TM-polarized light into the TM-selective resonator. The uncertainty originates mainly from a thermal-delay-induced deviation from the wavelength calibration. For a designed coupling gap of 700 nm at the middle of the coupler section, the TM-selective PSMR with a waveguide width of 900 nm exhibits notch resonances with an ER of 11 dB for TM-polarized input light, and no visible resonance for TE-polarized light [Fig. 5(c)]. The TE-selective PSMR shows resonances for both polarizations, but exhibits a strong ER contrast, ΔER , of 8.5 dB between TE- and TM-polarized input light [Fig. 5(d)]. Indeed, these results are highly consistent with the reduced PDCR observed in the TE-selective PSBTs measured earlier in this section. Strongly polarization-dependent resonant spectral manipulation is successfully implemented on an integrated platform, without requiring polarization-attenuating elements in the resonant cavity or any external PBS devices.

4. Conclusion

An approach to achieving broadband and highly efficient polarization-selective integrated photonics is proposed, simulated and validated with fabricated and characterized devices. At its core, it leverages a set of possible waveguiding configurations that are differentiated by spatially mapped optical anisotropy. By selecting an appropriate combination of states and employing smooth transitions between them, polarized light can be efficiently parsed over bandwidths that were previously inaccessible to integrated photonics.

Polarizing beam splitters (PBS) are investigated using this approach. A record fractional bandwidth of 0.52 octaves or 116 THz is demonstrated, while maintaining a minimum ER of 16 ± 3 dB and a maximum on-chip insertion loss of 1.4 ± 0.8 dB, exceeding the prior record in integrated PBS bandwidth by a factor of 4.

We also show how it can be used to enable novel photonic structures such as polarization-selective beam-taps and microring resonators. Such devices are designed using state-transitions in a similar way for the PBS. Beam-taps with coupling coefficients in the 1% range are shown to exhibit strong polarization selectivity up to 14 ± 1 dB in their coupling ratio. A TM-selective microring resonator is fabricated and characterized, showing deep notch resonances for TM-polarized light and completely suppressed resonance for TE-polarized light.

Further improvements to the planarization and etching are expected to drastically improve the performance in both loss and bandwidth. As it stands, this technology could be directly applied to realize ultra-broadband, compact and high-sensitivity polarimetric imagers using single-pixel imaging techniques [30]. Future investigation will also include multi-element polarimetric receivers. This technology shows significant promise for integrated polarization-diverse photonics for sensing and high-bandwidth communications.

Funding

National Science Foundation (NSF) CAREER (ECCS-1150672).

Acknowledgments

We thank A. Dogariu and C. Constant for loaning the 1117 nm laser source, neutral-density filters and polarizers. We also acknowledge S. Khan for assistance with the measurements.